

Interatomic potentials for hydrogen in α -iron based on density functional theory

Ashwin Ramasubramaniam*

*Program in Applied and Computational Mathematics, Princeton University, Princeton, New Jersey 08544, USA*Mitsuhiro Itakura[†]*Center for Computational Science and E-systems, Japan Atomic Energy Agency, 6-9-3 Higashiueno, Taito-ku, Tokyo 110-0015, Japan*Emily A. Carter[‡]*Department of Mechanical and Aerospace Engineering and Program in Applied and Computational Mathematics, Princeton University, Princeton, New Jersey 08544-5263, USA*

(Received 12 December 2008; revised manuscript received 25 March 2009; published 1 May 2009)

We present two interatomic potentials for hydrogen in α -iron based on the embedded atom method potentials for iron developed by Mendelev *et al.* [Philos. Mag. **83**, 3977 (2003)] and Ackland *et al.* [J. Phys.: Condens. Matter **16**, S2629 (2004)]. Since these latter potentials are unique among existing iron potentials in their ability to produce the same core structure for screw dislocations as density functional theory (DFT) calculations, our interatomic potentials for hydrogen in iron also inherit this important feature. We use an extensive database of energies and atomic configurations from DFT calculations to fit the cross interaction of hydrogen with iron. Detailed tests on the dissolution and diffusion of hydrogen in bulk α -iron, as well as the binding of H to vacancies, free surfaces, and dislocations, indicate that our potentials are in excellent overall agreement with DFT calculations.

DOI: [10.1103/PhysRevB.79.174101](https://doi.org/10.1103/PhysRevB.79.174101)

PACS number(s): 34.20.Cf, 02.70.Ns

I. INTRODUCTION

The deleterious effect of hydrogen on the mechanical properties of metals is a well-documented phenomenon.^{1–3} Although several microscopic mechanisms that govern the interaction of hydrogen with defects in metals have been uncovered through experimental work, the small size, high diffusivity, and low solubility of hydrogen in metals^{1,4} make direct observations an onerous task. With the steady increase in computing power and progress in the development of efficient algorithms, simulations at the atomic scale provide an attractive alternative. While first-principles quantum-mechanical calculations are undoubtedly the most accurate of such simulation methods, the high computational cost still renders them impractical for most material samples containing more than a few hundred atoms. Semi-empirical and empirical potentials provide a less accurate but more practical avenue for simulating more realistic system sizes containing millions of atoms. In an effort to improve accuracy and predictive capability, interatomic potentials increasingly are being fit to reproduce both experimental measurements of equilibrium properties as well as a range of equilibrium and nonequilibrium data from first-principles calculations. The purpose of this article is to present an interatomic potential for hydrogen in α -iron [body-centered cubic (bcc) structure] that is fit to an extensive set of density functional theory (DFT) calculations.

Interatomic potentials that capture the many-body aspects of metallic bonding have found wide applicability and success in simulations of metals. For hydrogen in α -iron in particular, embedded atom method (EAM) potentials^{5–7} have been developed by Ruda *et al.*⁸ and Wen *et al.*⁹ More recently, a modified embedded atom method (MEAM) potential for both bcc and fcc phases has been developed by Lee and Jang.¹⁰ The shortcomings of Ruda *et al.*'s potential, in

particular, its inability to predict the correct bulk interstitial site for H in α -Fe as well as its inability to produce accurate binding energies for H to vacancies, have been discussed before in Refs. 9 and 10. While Wen *et al.*'s potential is accurate in these aspects, we have shown in a recent publication¹¹ that this potential predicts an anomalously high energy barrier for H atoms to bind to a vacancy. This drawback results in elevated diffusion constants (10^3 – 10^4 times higher) at low temperatures for H in the presence of vacancy traps. The other main drawback of Wen *et al.*'s potential is related to the description of Fe-Fe interactions, which is based on Johnson and Oh's¹² analytical EAM potential. This potential predicts that a relaxed screw dislocation core spreads along three $\langle 112 \rangle$ directions to adopt a threefold degenerate structure. The newer MEAM potential¹⁰ also predicts the same threefold core structure for screw dislocations.¹³ In contrast, DFT calculations^{14,15} clearly indicate that the screw core remains compact with sixfold symmetry. Screw dislocations, because of their low mobility, are known to play an important role in plasticity in bcc metals. Hydrogen is known to enhance the mobility of dislocations and promote plasticity—the so-called hydrogen-enhanced local plasticity mechanism^{16,17}—eventually leading to localized plastic collapse and failure. To model the interaction of hydrogen with dislocations accurately, it is crucial that the dislocation itself be modeled accurately. To the best of our knowledge, among the myriad interatomic potentials developed for iron, only the ones developed by Mendelev *et al.*¹⁸ and Ackland *et al.*¹⁹ correctly predict the same compact sixfold core as DFT calculations.^{15,20} Therefore, we choose to develop potentials for H in α -Fe based on these Fe potentials.

The organization of this paper is as follows. In Sec. II we provide details of the DFT calculations and the parameterization procedure for interatomic potentials. In Sec. III we

provide a critical assessment of the performance of the interatomic potentials. In particular, we examine dissolution and diffusion of H in bulk α -Fe as well as binding of H to free surfaces, vacancies, and dislocations. Concluding remarks are provided in Sec. IV.

II. CALCULATIONAL DETAILS

A. DFT calculations

The details of the DFT calculations used to generate fitting targets for the interatomic potential have been reported previously in Ref. 11. We briefly recall the salient points here.

Spin-polarized DFT calculations are performed using the Vienna *Ab Initio* Simulation Package (VASP).^{21–23} Standard projector-augmented wave (PAW) potentials^{24,25} supplied with VASP are used to represent the nuclei plus core electrons up to the $3p$ shell for Fe and to represent the nuclei for H. Electron exchange and correlation are treated with the generalized gradient approximation (GGA) of the Perdew-Burke-Ernzerhof (PBE) form.²⁶ Bulk dissolution of hydrogen is modeled using a supercell containing 54 Fe atoms and 1 H atom (1.8 at. % H). We use a kinetic energy cutoff of 500 eV and a $6 \times 6 \times 6$ Monkhorst-Pack k -point mesh for this supercell. Brillouin zone integration is performed using the first-order Methfessel-Paxton method,²⁷ with a Fermi surface smearing of 0.1 eV. All structural relaxations are performed until forces on atoms are below 0.01 eV/Å. With these parameters, the total energy of the Fe₅₄ cell is converged to within 1 meV/atom and the dissolution energy (without atomic relaxation) of H in a tetrahedral site is converged to within 2 meV. Adsorption of H on Fe(100) and (110) surfaces is modeled using seven- and five-layer periodic slabs containing 63 and 60 Fe atoms,²⁸ respectively, with 10 Å of vacuum separating the periodic images of the slab in the direction normal to the free surfaces. In both cases, the H adatom and two Fe layers below it are relaxed while the other layers are held fixed at the bulk lattice constant. The maximum force on atoms in the layer immediately below the free layers is 0.06 eV/Å and 0.1 eV/Å for the Fe (100) and Fe (110) cells, respectively. Since the slab calculations require a much larger supercell than the bulk calculations, we use a smaller energy cutoff of 300 eV and a $4 \times 4 \times 1$ k -point mesh to reduce the computational cost; this choice of parameters has been shown to be sufficiently accurate in prior studies.^{29,30} Minimum energy pathways for bulk diffusion between tetrahedral (T) site minima are computed by the climbing image nudged elastic band method³¹ with a spring force constant of 5 eV/Å² between images. The rank of the saddle point is determined by diagonalizing a Hessian matrix with displacements of ± 0.02 Å. Since the much more massive Fe atoms couple weakly to the H atom, only the H atom is allowed to move in the Hessian construction. Zero-point corrections to dissolution energies are computed from the real-valued normal vibrational modes of the H atom.³²

B. Functional forms and fitting procedure for interatomic potentials

As noted previously, the potentials for H in α -Fe developed here are based on the Fe potentials developed by Men-

delev *et al.*¹⁸ and Ackland *et al.*¹⁹ Initially, Mendeleev *et al.* provided parameterizations for two potentials (Potential 2 and Potential 4 in Ref. 18). While both potentials were fit to perfect crystal and point defect data, Potential 2 was additionally fit to DFT forces whereas Potential 4 was fit to experimental liquid structure data. The relative merits of each potential are extensively discussed in the original paper. Subsequently, those authors further optimized Potential 2 using additional point defect data.¹⁹ In this work, we describe Fe-Fe interactions using the parameterization for Potential 4 from Ref. 18 (Potential A in this work) and for the improved Potential 2 from Ref. 19 (Potential B in this work). Our task then is to fit the Fe-H and H-H interactions.

We represent the total energy of a collection of N atoms as

$$U = \frac{1}{2} \sum_{i,j=1}^N \phi_{ij}(r_{ij}) + \sum_{j=1}^N F_j \left[\sum_{i=1}^N \rho_{ij}(r_{ij}) \right], \quad (1)$$

where r_{ij} is the distance between atoms i and j , ϕ_{ij} is the two-body interaction between atoms i and j , ρ_{ij} is the electron density contributed by atom i at atom j , and F_j is the embedding function for atom j . If $\rho_{ij} \equiv \rho_i$, i.e., the electron density depends only upon the “source” atom i and is independent of the “target” atom j , the above representation reduces to the well-known EAM form of Daw and Baskes.^{5–7} If the embedding function is chosen to be of the form $F(x) = -A\sqrt{x}$, the above representation reduces to the Finnis-Sinclair³³ form. As written here, Eq. (1) represents a general many-body form for the total energy of the system.³⁴ With this many-body form, nine functions, namely, ϕ_{FeFe} , ϕ_{FeH} , ϕ_{HH} , ρ_{FeFe} , ρ_{FeH} , ρ_{HH} , F_{Fe} , and F_{H} must be specified; of these, ϕ_{FeFe} , ρ_{FeFe} , and F_{Fe} are predetermined from the works of Mendeleev *et al.*¹⁸ and Ackland *et al.*¹⁹ The functional forms for the remaining six functions are discussed next.

We describe two-body Fe–H interactions by the function^{18,19,35,36}

$$\phi_{\text{FeH}} = \begin{cases} \frac{Z_{\text{Fe}} Z_{\text{H}} q_e^2}{r} \Phi\left(\frac{r}{r_s}\right), & \text{for } r < r_1 \\ e^{B_0 + B_1 r + B_2 r^2 + B_3 r^3 + B_4 r^4 + B_5 r^5}, & \text{for } r_1 \leq r \leq r_2 \\ \sum_{i=1}^{N^\phi} a_i^\phi (r_i^\phi - r)^3 H(r_i^\phi - r), & \text{for } r > r_2, \end{cases} \quad (2)$$

where Z_{Fe} and Z_{H} are the atomic numbers of Fe and H, respectively; q_e is the electronic charge; $H(\cdot)$ is the Heaviside step function; $r_s = 0.88534a_0 / (Z_{\text{Fe}}^{2/3} + Z_{\text{H}}^{2/3})$ is the screening length, a_0 being the Bohr radius; and

$$\Phi(x) = 0.1818e^{-3.2x} + 0.5099e^{-0.9423x} + 0.2802e^{-0.4029x} + 0.02817e^{-0.2016x}, \quad (3)$$

is the screening function. In Eq. (2), we have used Biersack and Ziegler's³⁵ universal screened-Coulomb function in the range $r < r_1$ and a cubic spline fit in the range $r > r_2$. In the range $r_1 \leq r \leq r_2$, we have interpolated between the universal

screening function and the spline fit, with the coefficients of the interpolating function chosen to ensure continuity of the function and its first and second derivatives at r_1 and r_2 .

For H-H interactions we use the functional form³⁷⁻³⁹

$$\phi_{\text{HH}} = \begin{cases} s(r)\{E_{\text{mol}}(r) - 2F_{\text{H}}[\rho_{\text{H}}(r)]\} + [1 - s(r)][C_{1,\phi_{\text{HH}}}f_{\text{cut}}(r) + C_{2,\phi_{\text{HH}}}\rho_{\text{HH}}(r)], & \text{for } r \leq r_{\text{cut,HH}} \\ 0, & \text{for } r > r_{\text{cut,HH}}, \end{cases} \quad (4)$$

where

$$s(r) = 0.5[1 - \tanh\{25(r - 0.9)\}], \quad (5)$$

$$E_{\text{mol}} = -2E_b(1 + a^\dagger)e^{-a^\dagger}, \quad (6)$$

$$f_{\text{cut}}(r) = e^{1/(r-r_{\text{cut,HH}})}, \quad (7)$$

$$a^\dagger = \frac{r - r_0}{r_0\lambda}. \quad (8)$$

In the above expressions, $E_b = 2.37$ eV/atom is the molecular bond strength of H_2 , $r_0 = 0.74$ Å is the H_2 equilibrium bond length, $\lambda = 0.4899$, $r_{\text{cut,HH}}$ is the cutoff distance for H-H two-body interactions, and ρ_{HH} is the H-H electron density, which will be described subsequently. As noted by Foiles *et al.*,³⁷ this functional form accurately describes the potential energy surface for molecular hydrogen near the equilibrium separation and rapidly switches to a short-ranged empirical potential description past 0.9 Å.

The embedding function for hydrogen is taken to be a polynomial in ρ of the form

$$F_{\text{H}}(\rho) = \sum_{i=1}^{N^F} a_i^F \rho^i. \quad (9)$$

Our attempts to use a Finnis-Sinclair description³³ for the embedding function [$F(x) = -A\sqrt{x}$ or generalizations thereof^{18,19}] did not provide sufficiently accurate fits. The simple polynomial form employed here yielded significantly better results.

For the electron-density functions, we found that the EAM approach of using charge densities that depend solely upon the “source” atomic species were insufficient to generate accurate parameterizations. Therefore, we adopted a more general approach wherein the electron density from the “source” atom i at the “target” atom j , denoted by ρ_{ij} , depends upon both species. This is similar to the Finnis-Sinclair approach except for the different functional form of the embedding function. Thus, in addition to the electron density ρ_{FeFe} for pure iron, we introduce three additional electron densities

$$\rho_{\text{FeH}} = \sum_{i=1}^{N^{\rho_{\text{FeH}}}} a_i^{\rho_{\text{FeH}}}(r_i^{\rho_{\text{FeH}}} - r)^3 H(r_i^{\rho_{\text{FeH}}} - r), \quad (10)$$

$$\rho_{\text{HFe}} = \sum_{i=1}^{N^{\rho_{\text{HFe}}}} a_i^{\rho_{\text{HFe}}}(r_i^{\rho_{\text{HFe}}} - r)^3 H(r_i^{\rho_{\text{HFe}}} - r), \quad (11)$$

$$\rho_{\text{HH}} = C_{\rho_{\text{HH}}} r^2 e^{-2r/a_0} f_{\text{cut}}(r). \quad (12)$$

The coefficients of ρ_{FeH} and ρ_{HFe} are determined by fitting to the database of dissolution and binding energies, as described below. The H-H electron density ρ_{HH} is constructed from the radial probability distribution for the $1s$ orbital, which is scaled by a factor $C_{\rho_{\text{HH}}}$ and multiplied by a cutoff function f_{cut} that causes the density to go to zero rapidly as $r \rightarrow r_{\text{cut,HH}}$. The rescaling coefficient $C_{\rho_{\text{HH}}}$ and the cutoff distance $r_{\text{cut,HH}}$ are adjusted manually to obtain reasonable dissolution energies and the correct overall trend (consistent with DFT calculations from Ref. 40) for multiple H atoms binding to a vacancy. As of now, we have not undertaken DFT studies of clusters of strongly interacting H atoms dissolved in bulk α -Fe; in principle, such configurations or even iron hydride could be used to improve the parameterization of ρ_{HH} as well as the long-range (>0.9 Å) part of ϕ_{HH} .

The coefficients of the various functions described above were determined by fitting to a database of dissolution energies and atomic configurations of H in α -Fe. In particular, we considered: (1) H in tetrahedral site minima and at saddle points for hops between tetrahedral sites in both strained and unstrained lattices, (2) H bound at vacancies and at saddle points for hops to vacancy binding sites, and (3) H bound to (100) and (110) surfaces. The optimal parameters were determined by a two-stage approach. In the first stage we used simulated annealing⁴¹ to minimize a cost function

$$\mathcal{E} = \sum_{i=1}^M [\lambda_i (E_{d,i}^{\text{DFT}} - E_{d,i})^2 + \mu_i |f_i^{\text{EAM}}|^2], \quad (13)$$

where M is the total number of atomic configurations; $E_{d,i}^{\text{DFT}}$ and $E_{d,i}$ are the dissolution energies⁴² of H in configuration i as computed with DFT and the interatomic potential, respectively; f_i^{EAM} is the $3N$ -vector of forces, obtained from the interatomic potential, acting on the N atoms in configuration i ; and $\lambda_i, \mu_i > 0$ are weighting parameters. In this initial stage we only used bulk and vacancy data as fitting targets without weighting the fits toward any particular configuration ($\lambda_i = \mu_i = 1$). The resulting potentials were found to perform satisfactorily in the bulk as well as at vacancies, as expected,

but were less than satisfactory at surface binding sites, thus indicating a lack of transferability. We then added surface properties to the fitting database and, starting from the simulated annealing parameters, performed a Broyden-Fletcher-Goldfarb-Shanno (BFGS) optimization procedure.⁴³ In this stage we placed extra emphasis upon (1) the bulk dissolution energy and energy barrier for hops in the unstrained lattice, (2) the vacancy binding energy, and (3) binding energies at surface sites. While the potentials showed some deterioration in bulk properties, we found a marked improvement in surface properties after the second stage of fitting. We defer a detailed discussion of the quality of the potentials to the next section.

Before concluding this section, a couple of remarks about the cost function [Eq. (13)] are in order. In particular, note that we minimize the magnitude of the *actual* $3N$ force vector $|f_i^{\text{EAM}}|^2$ and not the *residual* force vector $|f_i^{\text{DFT}} - f_i^{\text{EAM}}|^2$. In effect, we are fitting to *atomic positions* from DFT and not to DFT forces. The reason for doing so is as follows. Our DFT calculations (PAW-PBE-GGA) predict a lattice parameter of 2.834 Å for α -Fe, which is different from the lattice parameter (2.855 Å) of the Fe EAM potentials. This implies that an unstrained DFT cell is actually at about 0.7% compressive strain from the perspective of the EAM potential. Therefore, we rescaled all our relaxed DFT configurations to the EAM lattice parameter to eliminate the residual compressive strain. As a consequence though, we could no longer retain forces from the original DFT configuration in the new rescaled configuration. Hence, we chose to minimize the total force and not the residual force, thereby fitting to (rescaled) DFT atomic positions rather than to DFT forces.

III. RESULTS AND DISCUSSION

Following the fitting procedure noted in Sec. II B, we parameterized two interatomic potentials for H in α -Fe. Potential A is based on Potential 4 of Mendeleev *et al.*,¹⁸ where the latter was fit to perfect crystal, point defect, and experimental liquid structure data. Potential B is based on the Fe potential of Ackland *et al.*,¹⁹ where the latter was fit to perfect crystal and point defect data, as well as DFT forces. Numerical values for the various coefficients and plots of the two-body, density, and embedding functions are provided in the Appendix. We provide below a critical assessment of our Fe-H potentials. First, we examine dissolution and diffusion of H in strained bulk α -Fe. Next, we consider binding of H to (100) and (110) surfaces, paying careful attention to both the binding energies as well as the nature of the binding sites (minima/saddles). Thereafter, we study binding of single and multiple H atoms to vacancies as well as the barriers for attachment/detachment from vacancy binding sites. Finally, we examine the binding of H to screw and edge dislocations.

A. Strain-dependent dissolution and diffusion of H in bulk α -Fe

Experimental evidence suggests that H dissolves in tetrahedral (T) interstitial sites with a dissolution energy of 0.30 eV.¹ Recent DFT calculations^{30,40} indeed confirm that H

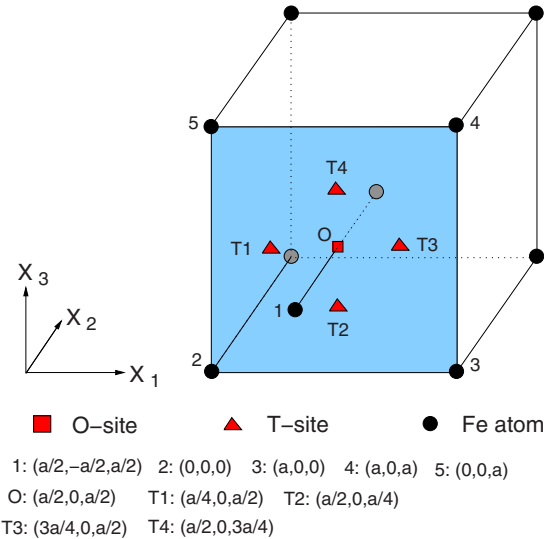


FIG. 1. (Color online) Schematic of bcc Fe lattice showing four tetrahedral sites and one octahedral site on a face.

preferentially dissolves in tetrahedral (T) sites, as opposed to octahedral (O) sites, with a dissolution energy of approximately 0.3 eV (corrected for quantum effects arising from zero-point vibrations). Furthermore, we have shown recently¹¹ that H preferentially dissolves in T-sites even when the Fe lattice is subjected to moderate strains, thereby indicating that site preference is unlikely to be altered except perhaps in the immediate vicinity of defects. Dissolution energies for H in a T-site (T1 in Fig. 1) as a function of hydrostatic and uniaxial strain are presented in Table I and displayed in Fig. 2.⁴⁶ Diffusion barriers for hops between T-sites (from T1 to T2 in Fig. 1) as a function of strain are also presented in Table I and displayed in Fig. 3. As noted in previous work³⁰ and seen from Table I, DFT calculations for diffusion barriers in unstrained cells are in good agreement with experimental values, thereby providing reliable fitting targets. For purposes of comparison, we also provide energies computed with Wen *et al.*'s⁹ EAM potential. Additionally, it is worth noting that the MEAM potential¹⁰ overestimates the energy barrier for bulk diffusion at zero strain by a factor of six.

As seen from Fig. 2, the strain-dependent dissolution energies in T-sites obtained with our interatomic potentials are in reasonable qualitative and quantitative agreement with DFT calculations. The disagreement with DFT becomes more apparent at compressive strains and could be due to stronger many-body effects under compression that are not adequately represented by empirical potentials.¹⁹ The diffusion barriers obtained with the interatomic potentials also show greater disagreement with DFT calculations under compression, as seen from Fig. 3. In particular, DFT predicts a diffusion barrier that is nearly independent of applied hydrostatic strain, in marked contrast with the interatomic potentials. Interestingly, when the potentials were only fit to bulk and vacancy data, the diffusion barriers were indeed found to be relatively insensitive to hydrostatic strain.⁴⁷ However, H adsorption at surfaces was found to be poorly described when only bulk data was used in the fit and so we

TABLE I. Comparison of interatomic potentials with PAW-PBE-GGA (fitting targets in italics) for dissolution and diffusion of H in bulk α -Fe. ϵ_h and ϵ_u are the strains applied to the Fe lattice for hydrostatic and uniaxial loading, respectively (see text). All energies are in eV.

	PAW-PBE-GGA	EAM ^a	Potential A	Potential B	Other
Dissolution energies					
ϵ_h					
+2%	<i>0.040</i>	0.140	0.059	0.061	
+1%	<i>0.180</i>	0.220	0.173	0.175	
0%	<i>0.330</i>	0.310	0.287	0.297	0.30 ^b , 0.35 ^c
-1%	<i>0.490</i>	0.420	0.403	0.430	
-2%	<i>0.670</i>	0.540	0.526	0.574	
ϵ_u					
+2%	<i>0.220</i>	0.220	0.205	0.208	
+1%	<i>0.270</i>	0.260	0.246	0.252	
-1%	<i>0.380</i>	0.340	0.328	0.343	
-2%	<i>0.430</i>	0.360	0.369	0.389	
Diffusion barriers					
ϵ_h					
+2%	<i>0.049</i>	0.046	0.040	0.042	
+1%	<i>0.048</i>	0.041	0.043	0.044	
0%	<i>0.045</i>	0.033	0.039	0.040	0.035–0.142 ^d , 0.042 ^e , 0.29 ^c
-1%	<i>0.046</i>	0.022	0.031	0.028	
-2%	<i>0.044</i>	0.007	0.015	0.007	
ϵ_u					
+2%	<i>0.012</i>	0.009	0.020	0.020	
+1%	<i>0.029</i>	0.018	0.029	0.030	
-1%	<i>0.067</i>	0.068	0.050	0.049	
-2%	<i>0.091</i>	0.115	0.062	0.059	

^aEAM parameters from Ref. 9.

^bExperiment, Ref. 1.

^cMEAM, Ref. 10.

^dExperiment, Ref. 44.

^eExperiment, Ref. 45.

had to add surface data to the training set. The potentials then showed improved behavior at surfaces but the energy barriers in the bulk deteriorated. Noting that (1) barriers for bulk diffusion are inherently small and (2) relative energetics

from DFT are reliable up to ± 20 meV, we accept errors ~ 30 meV in the diffusion barriers as a reasonable tradeoff for improved surface properties. Overall, from the RMS errors indicated in Figs. 2 and 3, Potential B is seen to be

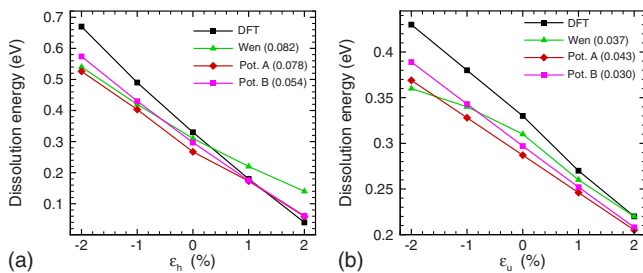


FIG. 2. (Color online) Dissolution energies of H in α -Fe as a function of (a) hydrostatic and (b) uniaxial strain. Numerical values in the legend indicate RMS errors for each potential with respect to DFT values. The lines are a guide to the eye.

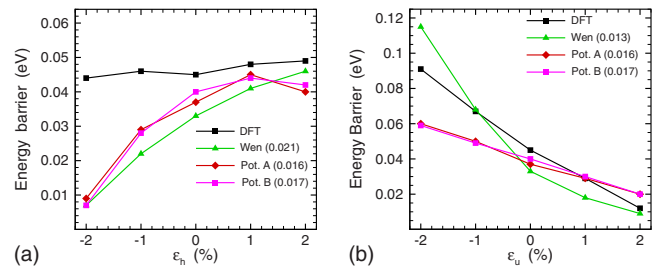


FIG. 3. (Color online) Diffusion barriers for H in α -Fe as a function of (a) hydrostatic and (b) uniaxial strain. Numerical values in the legend indicate RMS errors for each potential with respect to DFT values. The lines are a guide to the eye.

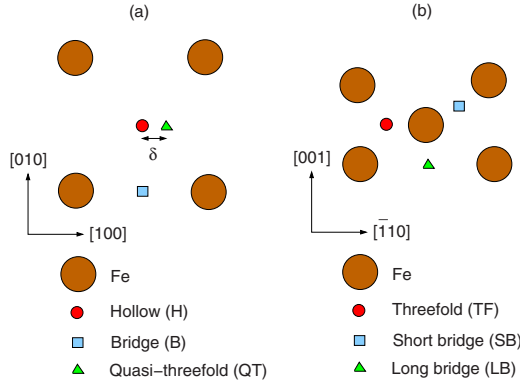


FIG. 4. (Color online) Schematic of possible binding sites for H on (a) Fe (100) and (b) Fe (110) surfaces.

slightly more accurate than Potential A.

B. Binding of H to free surfaces

As noted previously, Fe-H potentials derived from bulk and vacancy data alone were found to suffer from lack of

transferability to surfaces. To remedy this situation, we included DFT data for binding of H at various sites on (100) and (110) surfaces (Fig. 4) in the training set and re-optimized the potentials. We also ascertained stability of each binding site by diagonalizing the Hessian matrix with displacements of ± 0.02 Å; only the H atom was allowed to move in this procedure.

On the (100) surface, we examined binding at hollow, quasi-threefold, and bridge sites (Fig. 4). The binding energy E_b of an H atom to a surface is defined as $E_b = E_{d,T} - E_a$, where $E_{d,T}$ is the dissolution energy⁴² at a T-site in a perfect bulk crystal and E_a is the adsorption energy⁴² at a surface binding site. Previous DFT studies³⁰ indicate that hollow and bridge sites are both stable binding sites with the hollow site being favored by 0.04 eV. On accounting for zero-point corrections, which was not done in those DFT studies, we found that the hollow site was favored by 0.12 eV over the bridge site (see Table II). Based on a combination of electron energy loss spectroscopy and temperature programmed desorption, Merrill and Madix⁵¹ identified the fourfold hollow site as the preferred binding site at low H coverage. At higher coverage, they reported binding at asymmetric threefold sites (referred

TABLE II. Comparison of interatomic potentials with PAW-PBE-GGA (fitting targets in italics) for binding of H at (100) and (110) surfaces at coverages of 0.11 and 0.08 monolayers, respectively. The binding energy E_b of an H atom to a surface is defined as $E_b = E_{d,T} - E_a$ where $E_{d,T}$ is the dissolution energy (Ref. 42) at a T-site in a perfect bulk crystal and E_a is the adsorption energy (Ref. 42) at a surface binding site. “min” indicates stable minimum; “ts” indicates transition state; “hos” indicates higher-order saddle. All energies are in eV and distances in Å.

	PAW-PBE-GGA	EAM ^a	Potential A	Potential B	Other
Binding energies					
(100) surface					
Hollow	<i>0.775</i> (min)	0.627 (hos)	0.700 (hos)	0.717 (hos)	1.03 ^b , 0.82 ^c
Quasi-threefold	<i>0.768</i> (min)	0.628 (min)	0.727 (min)	0.749 (min)	
δ ^d	<i>0.19</i>	0.16	0.55	0.55	
Bridge	<i>0.655</i> (min)	0.624 (min)	0.665 (ts)	0.690 (ts)	
(110) surface					
Threefold	<i>1.003</i> (min)	0.630 (min)	0.672 (min)	0.734 (min)	1.22 ^b , 0.86 ^c
Long bridge	0.970 (ts) ^e	0.601 (ts)	0.624 (ts)	0.678 (ts)	
Short bridge	0.823 (ts) ^e	0.599 (min)	0.564 (ts)	0.621 (ts)	
Distance from surface to H					
(100) surface					
Hollow	<i>0.38</i>	0.20	0.20	0.21	
Quasi-threefold	<i>0.38</i>	0.43	0.28	0.29	
Bridge	<i>1.20</i>	0.74	0.74	0.74	
(110) surface					
Threefold	<i>0.98</i>	0.84	0.83	0.84	0.9 \pm 0.1 ^f
Long bridge	0.95 ^g	0.83	0.82	0.84	
Short bridge	1.14 ^g	1.05	0.83	0.84	

^aEAM parameters from Ref. 9.

^bMEAM, Ref. 10.

^cExperiment, Ref. 48.

^dDistance between hollow and quasi-threefold site (see Fig. 4).

^eZero-point corrections have been applied (Ref. 49) to values from Ref. 29.

^fExperiment, Ref. 50.

^gReference 29.

TABLE III. Comparison of interatomic potentials with PAW-PBE-GGA (fitting targets in italics) for trapping of one H atom at a vacancy. The binding energy E_b of an H atom to a vacancy is defined as $E_b = E_{d,T} - E_{d,v}$ where $E_{d,T}$ and $E_{d,v}$ are the dissolution energies (Ref. 42) at a T-site in a perfect bulk crystal and at a vacancy binding site, respectively. All energies are in eV and distances in Å.

	PAW-PBE-GGA	EAM ^a	Potential A	Potential B	Other
Binding energy	<i>0.690</i>	0.580	0.556	0.609	0.63 ^b , 0.56 ^c , 0.59 ^d
δ ^e	<i>0.23</i>	0.40	0.33	0.30	0.40 ^b , 0.26 ^d
Barrier: V + H _{T-site} → VH	<i>0.033</i>	0.110	0.042	0.025	
Barrier: VH → V + H _{T-site}	<i>0.650</i>	0.690	0.529	0.539	
Barrier: VH ↔ VH	<i>0.230</i>	0.050	0.061	0.061	

^aEAM parameters from Ref. 9.

^bExperiment, Ref. 2.

^cUSPP-GGA, Ref. 40.

^dMEAM, Ref. 10.

^eDistance between O-site and vacancy binding site (see Fig. 5).

to as quasi-threefold sites here) within the fourfold hollow, the former becoming dominant at saturation coverages. This quasi-threefold binding site had been identified previously by Blyholder *et al.*,⁵² who studied H on Fe clusters using semi-empirical quantum chemistry methods (MINDO/SR), as the strongest binding site on Fe(100). However, those calculations also predicted the bridge site to be a stronger binding site than the hollow site by 0.2 eV, which is in direct disagreement with more accurate DFT calculations.³⁰ Therefore, we independently performed DFT calculations to ascertain the possibility of binding at quasi-threefold sites. An H atom was inserted at a threefold position above the (100) surface and relaxed along with the top two layers of the Fe slab. During relaxation the H atom moved away from the threefold location and found a local minimum at a distance $\delta = 0.19$ Å from the hollow site (Fig. 4). A frequency analysis revealed this site to be a stable minimum. From Table II, we see that binding energies at the quasi-threefold and hollow sites differ by a mere 7 meV; since this energy difference is within the uncertainty of the DFT calculation (± 20 meV), we cannot conclusively assert the location of the strongest binding site on the (100) surface. We now note from Table II that our interatomic potentials clearly favor binding at the quasi-threefold site over the hollow site by about 30 meV, the latter additionally being a higher-order saddle rather than a local minimum. Overall, the binding energies are seen to be in good agreement with DFT calculations, but the nature of two of the critical points is predicted incorrectly by our potentials. Our potentials also underestimate the distance of the binding sites from the (100) surface in comparison with DFT.

On the (110) surface, we examined binding at threefold, long-bridge, and short-bridge sites (Fig. 4). We see from Table II that our potentials correctly predict both the ordering as well as the nature of binding sites. However, binding is 0.1–0.2 eV weaker than predicted from DFT calculations. Our potentials, once again, underestimate the distance of the binding sites from the (110) surface in comparison with DFT. Also, note that the binding energy at the Fe(110) threefold site is predicted to be slightly *lower* than that at the Fe(100) quasi-threefold site (by 50 meV and 15 meV for Potentials A and B, respectively) in disagreement with DFT calculations.

Our attempts at making the Fe(110) threefold site a stronger binding site than the Fe(100) quasi-threefold site consistently resulted in the Fe(100) bridge site becoming the strongest binding site [followed by (110) threefold and (100) quasi-threefold]. The cause of this discrepancy is not immediately clear although we speculate that this could be closely related to the behavior of the Fe potential at surfaces. In particular, Potential A (derived from Potential 4 of Mendeleev *et al.*¹⁸) predicts surface energies of 2.01 J/m² and 1.93 J/m² for (100) and (110) surfaces, respectively; Potential B (derived from Ackland *et al.*¹⁹) predicts surface energies of 1.75 J/m² and 1.65 J/m² for (100) and (110) surfaces, respectively. DFT calculations⁵³ using ultrasoft pseudopotentials (USPP) within GGA predict nearly degenerate surface energies of 2.29 J/m² and 2.27 J/m² for (100) and (110) surfaces, respectively. While the relative difference between (100) and (110) surface energies from the interatomic potentials is admittedly small, it might still be necessary to modify the original Fe potential itself to obtain the right ordering of (100) and (110) H-binding sites, which is, however, beyond the scope of this work. It is worth emphasizing that *for a particular surface alone*, our Fe-H potentials are in reasonable agreement with DFT calculations.

TABLE IV. Binding energy (in eV) for multiple hydrogen atoms at a vacancy. The binding energy, as tabulated here, is the energy required to trap an additional H atom at the vacancy, referenced to the bulk dissolution energy, i.e., $E_b = [E(\text{Fe}_m\text{H}) - E(\text{Fe}_m)] - [E(\text{Fe}_{m-1}\text{H}_n) - E(\text{Fe}_{m-1}\text{H}_{n-1})]$.

No. of trapped H	USPP-GGA ^a	EAM ^b	Potential A	Potential B
1	0.559	0.586	0.556	0.609
2	0.612	0.550	0.557	0.609
3	0.399	0.369	0.398	0.432
4	0.276	0.301	0.258	0.299
5	0.335	0.207	0.293	0.242
6	-0.019	0.109	0.174	0.084

^aReference 40.

^bWen *et al.*, Ref. 9.

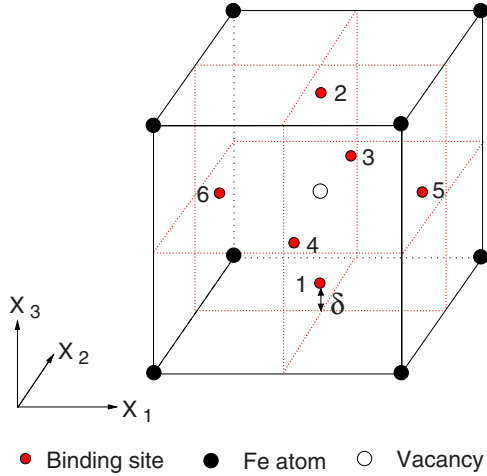


FIG. 5. (Color online) Schematic of H-binding sites at a vacancy. The binding site is displaced by δ from the O-site toward the vacancy. The numbering of the binding sites indicates the sequence in which H atoms are added to compute the binding energy for the $(n+1)$ th H atom (see text).

In summary, as far as binding energies on Fe(100) are concerned, our potentials are in better agreement with DFT than Wen *et al.*'s potential. However, our potentials predict the (100) bridge site to be a transition state unlike DFT or Wen *et al.*'s potential. This is not a major issue since the bridge site is not occupied even at high coverages; the four-fold hollow and quasi-threefold sites are the preferred binding sites. The main disagreement between our potentials and DFT arises for the position of the quasi-threefold site, which Wen *et al.*'s potential is apparently better at capturing. We do not have any obvious explanation for this. As noted before, our attempts at capturing the position of the quasi-threefold site more accurately led to deterioration of bulk properties, most notably the barrier for hops from bulk T-sites to the vacancy binding site (which, incidentally, Wen *et al.*'s potential significantly overestimates). On the Fe(110) surface, all potentials considered here tend to underestimate the binding energy. Additional optimization of the Fe potential itself might help resolve these remaining discrepancies.

C. Trapping of H at vacancies

We consider first the binding of a single H atom at a vacancy. The binding energy E_b of an H atom to a vacancy is

TABLE V. Binding energy (in eV) for hydrogen atoms at a dislocation core. The binding energy E_b of an H atom to a dislocation core is defined as $E_b = E_{d,T} - E_{d,c}$ where $E_{d,T}$ and $E_{d,c}$ are the dissolution energies (Ref. 42) at a T-site in a perfect bulk crystal and at a dislocation core binding site, respectively.

	Potential A	Potential B	Other
Screw	0.26	0.29	0.17 ^a , 0.44 ^b
Edge	0.37	0.42	0.46 ^a , 0.47 ^b

^aMEAM, Ref. 10.

^bEAM, Ref. 9.

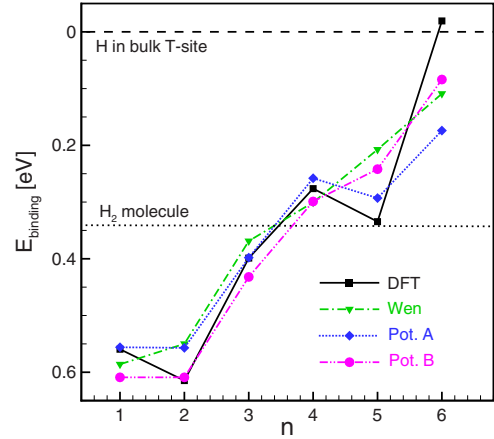


FIG. 6. (Color online) Binding energy (in eV) for multiple hydrogen atoms at a vacancy. The binding energy, as displayed here, is the energy required to trap an additional H atom at the vacancy, referenced to the bulk dissolution energy, i.e., $E_b = [E(\text{Fe}_m\text{H}) - E(\text{Fe}_m)] - [E(\text{Fe}_{m-1}\text{H}_n) - E(\text{Fe}_{m-1}\text{H}_{n-1})]$. Dissolution of up to three H atoms is seen to be exothermic (referenced to bulk Fe and H_2). Trapping at a vacancy, even in the presence of other trapped atoms, is almost always less endothermic than dissolution in a bulk T-site.

defined as $E_b = E_{d,T} - E_{d,v}$, where $E_{d,T}$ and $E_{d,v}$ are the dissolution energies⁴² at a T-site in a perfect bulk crystal and at a vacancy binding site, respectively. As seen from Table III, all the interatomic potentials produce binding energies in reasonable agreement with the experimental value of 0.63 eV and within the range (0.56–0.69 eV) established by DFT calculations. The displacement of the H atom from the O-site toward the vacancy (Fig. 5) is also found to be in reasonable agreement with DFT calculations and experimental estimates. In both cases, Potential B is in better agreement with the target DFT values than Potential A. The barriers for hops to a vacancy binding site from a bulk T-site ($\text{V} + \text{H}_{\text{T-site}} \rightarrow \text{VH}$) as computed with our potentials are in significantly better agreement with DFT values than from Wen *et al.*'s EAM potential. In particular, Potential B even captures the downhill trend for diffusion barriers (see Tables I and III) as the H atom approaches the vacancy. Therefore, H atoms now can be trapped readily by vacancies without being reflected by the unphysically high barrier predicted by

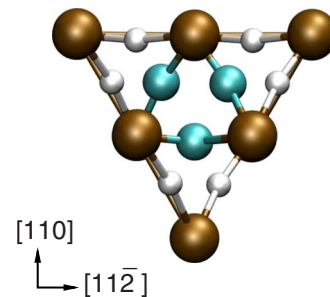


FIG. 7. (Color online) Binding sites for H atoms at a screw dislocation core. The blue and white spheres represent the first and second shell of binding sites around the core. The “bonds” are merely a guide for visualization.

TABLE VI. Parameters for two-body functions ϕ_{FeH} and ϕ_{HH} . Energies and distances are in eV and Å, respectively.

Parameter	Potential A	Potential B
	ϕ_{FeH}	
r_1	0.6	0.6
r_2	1.2	1.2
a_1^ϕ, r_1^ϕ	14.0786236789212005, 1.6	14.0786236766230779, 1.6
a_2^ϕ, r_2^ϕ	-4.4526835887173704, 1.7	-4.4526835638887965, 1.7
a_3^ϕ, r_3^ϕ	5.5025121262565992, 1.8	5.5025349784052979, 1.8
a_4^ϕ, r_4^ϕ	-1.0687489808214079, 2.0	-1.0687331741292405, 2.0
a_5^ϕ, r_5^ϕ	-0.3461498208163201, 2.5	-0.3461226670484926, 2.5
a_6^ϕ, r_6^ϕ	-0.0064991947759021, 3.2	-0.0064991313802717, 3.2
a_7^ϕ, r_7^ϕ	-0.0357435602984102, 4.2	-0.0357322844877736, 4.2
B_0	853.4769964964161	768.3086200576429
B_1	-4206.406420131467	-3648.143544963435
B_2	8686.215689507188	7262.725343225208
B_3	-9137.341019760202	-7381.290150466884
B_4	4807.823405345844	3764.3556602873186
B_5	-1002.9040584960112	-763.7887293847041
	ϕ_{HH}	
$C_{1,\phi_{\text{HH}}}$	0.0	0.0
$C_{2,\phi_{\text{HH}}}$	0.0	0.0
$r_{\text{cut},\phi_{\text{HH}}}$	2.3	2.4

Wen *et al.*'s potential that results in spurious elevated diffusivities at low temperatures.¹¹ The energy barrier for unbinding from a vacancy ($\text{VH} \rightarrow \text{V} + \text{H}_{\text{T-site}}$) is less well reproduced with our potentials, the error being about 0.12 eV. However, since the barrier for unbinding is relatively large to begin with (0.65 eV) and, furthermore, since the effective diffusivity of H is determined only by the trap-binding energy,^{54,55} this error is likely to be of less consequence. Lastly, we note that none of the interatomic potentials accurately capture the large barrier for hops between vacancy binding sites ($\text{VH} \leftrightarrow \text{VH}$), the energies typically being about 3–4 times smaller than DFT estimates. Tateyama and Ohno⁴⁰ showed that H atoms trapped at the vacancy saturate Fe broken bonds through the formation of Fe 3*d*-H 1*s* bonds. To accomplish a hop from one vacancy binding site to another these bonds must first be broken, which then explains the relatively large energy barrier for the process. In general though, such bond-formation and bond-breaking processes cannot be accurately captured with the class of interatomic potentials used in this work.

Next, we consider the binding of multiple H atoms to a vacancy. The sequence in which H atoms are assumed to be trapped at the vacancy is indicated by the numbering in Fig. 5. In Table IV, we present the binding energy of the ($n+1$)th H atom at a vacancy; the same data are displayed in Fig. 6. Suppose that H-H interactions are described purely by the short-ranged pair potential ϕ_{HH} . Since nearest-neighbor vacancy binding sites are nearly 2 Å apart, direct two-body H-H interactions are negligible (weakly attractive); therefore, H atoms only interact indirectly via the Fe lattice. This indirect interaction is also sufficiently weak such that the binding energy for each additional H atom was found to be nearly

constant in our initial potentials. However, DFT calculations⁴⁰ indicate that the binding energy decreases nearly monotonically with increasing H trapping (see Fig. 6), underscoring the importance of H-H coupling. Therefore, we include in our potentials an H-H density term ρ_{HH} , whose functional form has been noted previously in Sec. II B. This additional density now appears in the embedding function $F_H(\rho)$ and enhances direct H-H interactions. By adjusting

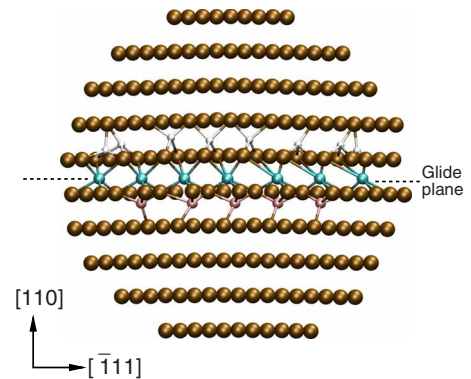


FIG. 8. (Color online) Binding sites for H atoms at an edge dislocation core. The extra half-plane of atoms is above the glide plane thus making the stresses compressive (tensile) above (below) the glide plane. The lowest-energy binding sites along the glide plane are indicated in blue (octahedral coordination). The pink spheres (tetrahedral coordination) represent weak binding sites immediately below the glide plane of the dislocation. The white spheres (tetrahedral coordination) represent sites with negative binding energy, i.e., dissolution is less energetically favorable than at a bulk T-site. The “bonds” are merely a guide to viewing the coordination.

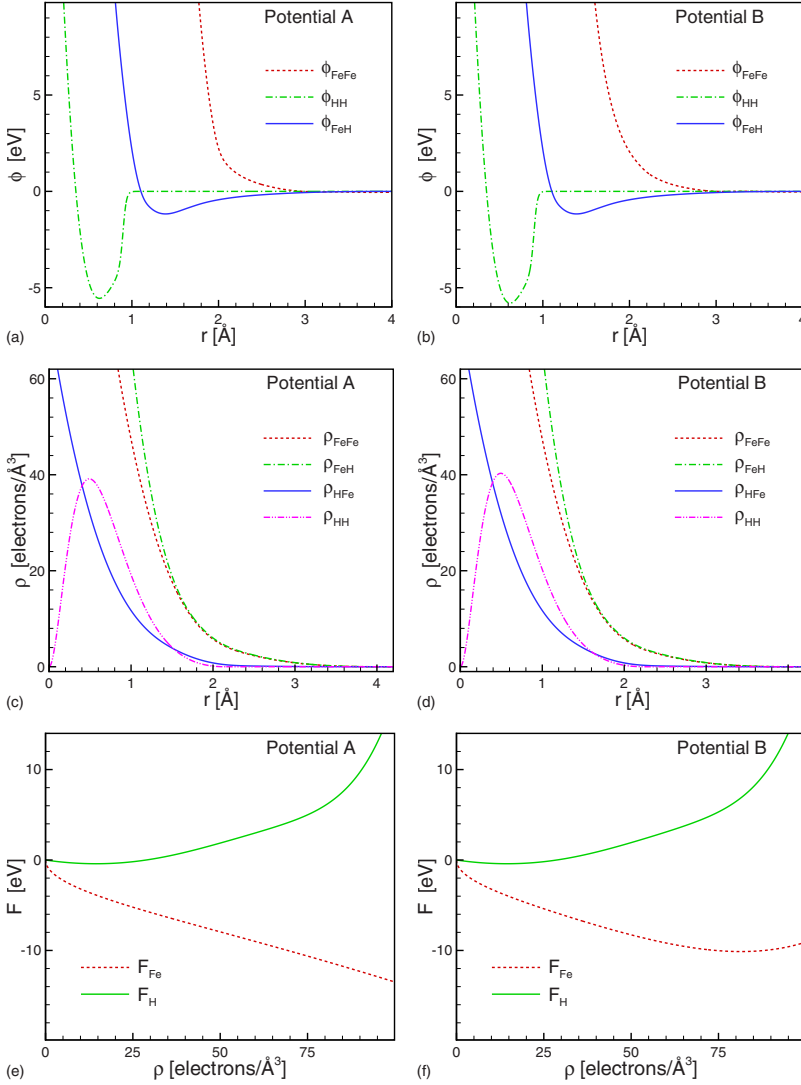


FIG. 9. (Color online) (a) Two-body, (b) electron density, and (c) embedding functions for Potentials A and B.

$C_{\rho_{\text{HH}}} > 0$, the interaction between H atoms can be made sufficiently repulsive to reproduce the overall trend of DFT calculations, as seen in Fig. 6. At the same time, by adjusting $r_{\text{cut,HH}}$ to be sufficiently small, i.e., nearly equal to the distance between diametrically opposite binding sites, repulsion between H atoms bound at these sites can be avoided. DFT calculations⁴⁰ (see Table IV) indicate that it is energetically favorable (exothermicity of 50 meV) for a VH complex to trap a second H atom at a site diametrically opposite to the initially occupied binding site. Following the strategy outlined above, we were able to make the binding energy of a second H atom to a VH complex *equal* to that for binding of an H atom to vacancy. Ideally, we would have liked to obtain a stronger binding energy for the second H atom than the first, but the only way to achieve this within the present formulation is to make H-H interactions weakly attractive at long distances. However, preliminary molecular dynamics tests reveal that this *ad-hoc* fix leads to other problems such as causing H atoms to desorb from surfaces and cluster in the gas phase. Therefore, we accept for now this slight discrepancy in our potentials whereby there is no additional energetic preference to trap a second H atom at a VH complex. Interestingly, we find that Potential A automatically repro-

duces the nonmonotonic behavior in the binding energy curve at $n=5$, in qualitative agreement with DFT calculations.

D. Trapping of H at dislocations

We introduced equi-spaced screw and edge dislocations in a periodic quadrupolar configuration in a bulk α -Fe simulation cell. We chose a unit cell (six atoms) with edges of lengths $a\sqrt{3}/2$, $a\sqrt{6}$, and $a\sqrt{2}$ along the $[\bar{1}11]$, $[11\bar{2}]$, and

TABLE VII. Parameters for hydrogen embedding function F_H . Energies and distances are in eV and Å, respectively.

Parameter	Potential A	Potential B
a_1^F	-0.0581256120818134	-0.0581047132616673
a_2^F	0.0022854552833736	0.0022873205657864
a_3^F	-0.0000314202805805	-0.0000313966169286
a_4^F	0.0000013764132084	0.0000013788174098
a_5^F	-0.0000000253707731	-0.0000000253074673
a_6^F	0.0000000001483685	0.0000000001487789

TABLE VIII. Parameters for electron density functions ρ_{FeH} , ρ_{HFe} , and ρ_{HH} . Energies and distances are in eV and Å, respectively.

Parameter	Potential A	Potential B
	ρ_{FeH}	
$a_1^{\rho_{\text{FeH}}}, r_1^{\rho_{\text{FeH}}}$	10.0073629216300581, 1.6	10.0073629218346891, 1.6
$a_2^{\rho_{\text{FeH}}}, r_2^{\rho_{\text{FeH}}}$	32.4861983261490295, 1.8	32.4862873850836635, 1.8
$a_3^{\rho_{\text{FeH}}}, r_3^{\rho_{\text{FeH}}}$	-0.9494226032063788, 2.0	-0.9494211670931015, 2.0
$a_4^{\rho_{\text{FeH}}}, r_4^{\rho_{\text{FeH}}}$	11.6659812262450338, 2.4	11.6683860903729624, 2.4
$a_5^{\rho_{\text{FeH}}}, r_5^{\rho_{\text{FeH}}}$	-0.0147080251458273, 3.2	-0.0147079871493827, 3.2
$a_6^{\rho_{\text{FeH}}}, r_6^{\rho_{\text{FeH}}}$	0.4943383753319843, 4.2	0.4945807618408609, 4.2
	ρ_{HFe}	
$a_1^{\rho_{\text{HFe}}}, r_1^{\rho_{\text{HFe}}}$	11.1667357634216433, 1.5	11.1667357634216433, 1.5
$a_2^{\rho_{\text{HFe}}}, r_2^{\rho_{\text{HFe}}}$	-3.0351307365078730, 2.0	-3.0351469477486712, 2.0
$a_3^{\rho_{\text{HFe}}}, r_3^{\rho_{\text{HFe}}}$	3.6096144794370653, 2.5	3.6092404272928578, 2.5
$a_4^{\rho_{\text{HFe}}}, r_4^{\rho_{\text{HFe}}}$	0.0212509034775648, 3.0	0.0212508491354509, 3.2
$a_5^{\rho_{\text{HFe}}}, r_5^{\rho_{\text{HFe}}}$	0.0303914939946250, 4.2	0.0303904795842773, 4.2
	ρ_{HH}	
$C_{\rho_{\text{HH}}}$	1800	1800

[110] directions, respectively, a being the lattice constant of α -Fe. The simulation cells for screw and edge quadrupoles were created by repeating this unit cell $3 \times 40 \times 60$ times (43200 atoms) and $150 \times 1 \times 92$ (82800 atoms) along the $[\bar{1}11]$, $[11\bar{2}]$, and $[110]$ directions. Dislocations were introduced by displacing atoms according to the isotropic linear elastic fields.⁵⁶ The dislocated cells were relaxed in LAMMPS,⁵⁷ with a force tolerance of 0.001 eV/Å. Thereafter, an H atom was introduced at a putative binding site at the dislocation core and the cell was relaxed once again to compute the binding energy of the H atom. It is worth noting that the screw dislocation core, which is sixfold and nondegenerate with Mendeleev *et al.*'s and Ackland *et al.*'s Fe potentials, retains this structure even in the presence of a bound H atom, i.e., perturbations from the H atom do not lead to threefold spreading of the core. The energies for the strongest binding sites at the core are tabulated in Table V. For edge dislocations, Potential B is seen to be in better agreement with previous MEAM and EAM calculations than Potential A. It is worth emphasizing that dislocation configurations were not used in the training sets and, hence, these binding energies represent unbiased predictions from our potentials.

In addition to the strongest binding sites, we also examined a few other binding sites around the dislocation core. For the screw dislocation, sites in the second shell (Fig. 7) are found to have a slightly lower binding energy (by 0.02 eV) than the first shell with Potential A whereas the two shells are degenerate with Potential B. Higher shells have negligible binding energy, i. e., no preference exists for binding to such sites relative to unstrained bulk T-sites. For the edge dislocation, we computed binding energies at sites just above (compressive region) and below (tensile region) the glide plane in the core region (Fig. 8). As expected, sites just below the glide plane are weak trapping sites with binding energies of approximately 0.3 eV, whereas sites just above the glide plane have binding energies of approximately

-0.04 eV (i.e., dissolution is less favored than at a bulk T-site). We have not yet computed diffusion pathways and rates along dislocation cores, which will be undertaken in the future.

IV. CONCLUDING REMARKS

In summary, we have developed two interatomic potentials for modeling H in α -Fe. Our potentials are based on the EAM potentials of Mendeleev *et al.*¹⁸ and Ackland *et al.*,¹⁹ which have the unique ability to produce the same core structure for screw dislocations in α -Fe as DFT calculations. We used an extensive database of energies and atomic configurations from DFT calculations to fit the cross interaction of H and Fe. Detailed tests were carried out to ascertain the quality of our potentials with respect to the dissolution and diffusion of H in bulk α -Fe as well as the binding of H to vacancies, free surfaces, and dislocations. The overall agreement of our potentials with DFT calculations is very encouraging and suggests that these potentials might be used with confidence in the future to simulate H-defect interactions, grain-boundary diffusion, and hydrogen embrittlement of iron, among other problems. Between the two potentials developed in this work, Potential B is seen to reproduce DFT fitting targets with slightly greater accuracy than Potential A, although both potentials present several improvements over existing Fe-H potentials. Therefore, the choice of which potential to employ is probably best decided on the basis of the properties of Fe (see Refs. 18 and 19) that one wishes to model with greater accuracy.

ACKNOWLEDGMENTS

Computational resources were provided by the Arctic Region Supercomputing Center and the Maui High Performance Computing center. A.R. and E.A.C. gratefully ac-

knowledge financial support from the Office of Naval Research.

APPENDIX: PARAMETERS FOR INTERATOMIC POTENTIALS

The functional forms of the interatomic potentials and the fitting procedure have been discussed previously in the text.

Numerical parameters for Fe-H and H-H interactions are provided in Tables VI–VIII; parameters for Fe-Fe interactions for Potential A and Potential B are taken from Ref. 18 (Potential 4 in that work) and Ref. 19, respectively. The two-body, embedding, and electron density functions are displayed in Fig. 9. Potential files formatted for LAMMPS may be downloaded from <http://www.princeton.edu/mae/people/faculty/carter/homepage/research/potentials>.

*aramasub@princeton.edu

†itakura.mitsuhiro@jaea.go.jp

‡eac@princeton.edu

- ¹J. P. Hirth, *Metall. Trans. A* **11**, 861 (1980).
- ²S. M. Myers, M. I. Baskes, H. K. Birnbaum, J. W. Corbett, G. G. DeLeo, S. K. Estreicher, E. E. Haller, P. Jena, N. M. Johnson, R. Kirchheim, S. J. Pearton, and M. J. Stavola, *Rev. Mod. Phys.* **64**, 559 (1992).
- ³R. A. Oriani, *Annu. Rev. Mater. Sci.* **8**, 327 (1978).
- ⁴Y. Fukai, *The Metal-Hydrogen System*, Springer Series in Materials Science, 2nd ed. (Springer, Berlin, 2005).
- ⁵M. S. Daw and M. I. Baskes, *Phys. Rev. Lett.* **50**, 1285 (1983).
- ⁶M. S. Daw and M. I. Baskes, *Phys. Rev. B* **29**, 6443 (1984).
- ⁷M. S. Daw, S. M. Foiles, and M. I. Baskes, *Mater. Sci. Rep.* **9**, 251 (1993).
- ⁸M. Ruda, D. Farkas, and J. Abriata, *Phys. Rev. B* **54**, 9765 (1996).
- ⁹M. Wen, X.-J. Xu, S. Fukuyama, and K. Yokogawa, *J. Mater. Res.* **16**, 3496 (2001).
- ¹⁰B.-J. Lee and J.-W. Jang, *Acta Mater.* **55**, 6779 (2007).
- ¹¹A. Ramasubramaniam, M. Itakura, M. Ortiz, and E. A. Carter, *J. Mater. Res.* **23**, 2757 (2008).
- ¹²R. A. Johnson and D. J. Oh, *J. Mater. Res.* **4**, 1195 (1989).
- ¹³B.-J. Lee and Y.-M. Kim (private communication).
- ¹⁴S. L. Frederiksen and K. W. Jacobsen, *Philos. Mag.* **83**, 365 (2003).
- ¹⁵C. Domain and G. Monnet, *Phys. Rev. Lett.* **95**, 215506 (2005).
- ¹⁶C. D. Beachem, *Metall. Trans.* **3**, 437 (1972).
- ¹⁷H. K. Birnbaum and P. Sofronis, *Mater. Sci. Eng., A* **176**, 191 (1994).
- ¹⁸M. I. Mendeleev, S. Han, D. J. Srolovitz, G. J. Ackland, D. Y. Sun, and M. Asta, *Philos. Mag.* **83**, 3977 (2003).
- ¹⁹G. J. Ackland, M. I. Mendeleev, D. J. Srolovitz, S. Han, and A. V. Barashev, *J. Phys. Condens. Matter* **16**, S2629 (2004).
- ²⁰L. Ventelon and F. Williame, *J. Comput.-Aided Mater. Des.* **14**, 85 (2007).
- ²¹G. Kresse and J. Hafner, *Phys. Rev. B* **48**, 13115 (1993).
- ²²G. Kresse and J. Furthmüller, *Comput. Mater. Sci.* **6**, 15 (1996).
- ²³G. Kresse and J. Furthmüller, *Phys. Rev. B* **54**, 11169 (1996).
- ²⁴P. E. Blochl, *Phys. Rev. B* **50**, 17953 (1994).
- ²⁵G. Kresse and D. Joubert, *Phys. Rev. B* **59**, 1758 (1999).
- ²⁶J. P. Perdew, K. Burke, and M. Ernzerhof, *Phys. Rev. Lett.* **77**, 3865 (1996).
- ²⁷M. Methfessel and A. T. Paxton, *Phys. Rev. B* **40**, 3616 (1989).
- ²⁸This leads to a coverage of 0.11 and 0.08 monolayers of H for Fe (100) and Fe (110), respectively.
- ²⁹D. E. Jiang and E. A. Carter, *Surf. Sci.* **547**, 85 (2003).
- ³⁰D. E. Jiang and E. A. Carter, *Phys. Rev. B* **70**, 064102 (2004).
- ³¹G. Henkelman, B. Uberuaga, and H. Jónsson, *J. Chem. Phys.* **113**, 9901 (2000).
- ³²All DFT energies reported in this paper are corrected for zero-point vibrations unless explicitly noted otherwise. The interatomic potentials are fit to these zero-point corrected energies and hence do not need any further zero-point corrections.
- ³³M. W. Finnis and J. E. Sinclair, *Philos. Mag. A* **50**, 45 (1984).
- ³⁴In our initial attempts at potential development, we tried both the EAM and Finnis-Sinclair forms but the resulting potentials were unsatisfactory. We found that the flexibility afforded by a more general many-body form, in particular, the ability to use two different density functions ρ_{FeFe} and ρ_{FeH} , allowed for significantly improved results.
- ³⁵J. P. Biersack and J. F. Ziegler, *Nucl. Instrum. Methods Phys. Res.* **194**, 93 (1982).
- ³⁶G. J. Ackland, D. J. Bacon, A. F. Calder, and T. Harry, *Philos. Mag. A* **75**, 713 (1997).
- ³⁷S. M. Foiles, M. I. Baskes, C. F. Melius, and M. S. Daw, *J. Less-Common Met.* **130**, 465 (1987).
- ³⁸J. E. Angelo, N. R. Moody, and M. I. Baskes, *Modell. Simul. Mater. Sci. Eng.* **3**, 289 (1995).
- ³⁹M. I. Baskes, X. Sha, J. E. Angelo, and N. R. Moody, *Modell. Simul. Mater. Sci. Eng.* **5**, 651 (1997).
- ⁴⁰Y. Tateyama and T. Ohno, *Phys. Rev. B* **67**, 174105 (2003).
- ⁴¹S. Kirkpatrick, C. D. Gelatt, and M. P. Vecchi, *Science* **220**, 671 (1983).
- ⁴²The dissolution energy E_d of an H atom in a simulation cell containing n Fe atoms is defined as $E_d = E(\text{Fe}_n\text{H}) - E(\text{Fe}_n) - E(\text{H}_2)/2$. The adsorption energy at a surface binding site is defined in the same manner.
- ⁴³W. H. Press, S. A. Teukolsky, W. T. Vetterling, and B. P. Flannery, *Numerical Recipes in C*, 2nd ed. (Cambridge University Press, Cambridge, UK, 1992).
- ⁴⁴Y. Hayashi and W. M. Shu, *Solid State Phenom.* **73-75**, 65 (2000).
- ⁴⁵H. J. Grabke and E. Riecke, *Mater. Technol.* **34**, 331 (2000).
- ⁴⁶Hydrostatic loading is applied by subjecting the Fe lattice at equilibrium to a deformation gradient $\mathbf{F} = (1 + \epsilon_n)\mathbf{I}$, where \mathbf{I} is the identity tensor. Uniaxial loading is applied via a deformation gradient $\mathbf{F} = \mathbf{I} + \epsilon_u \mathbf{e}_2 \otimes \mathbf{e}_2$, where \mathbf{e}_2 refers to the unit vector along the x_2 direction in Fig. 1 and \otimes indicates the tensor product.
- ⁴⁷Parameterizations for potentials fit only to bulk and vacancy data are available at <http://www.princeton.edu/mae/people/faculty/carter/homepage/research/potentials>.
- ⁴⁸J. Krüger, H. D. Kunze, and E. Schürmann, in *Gas and Carbon in Metals*, edited by E. Fromm and E. Gebhardt (Springer, New

- York, 1976), p. 578.
- ⁴⁹D. E. Jiang (private communication).
- ⁵⁰W. Moritz, R. Imbihl, R. J. Behm, G. Ertl, and T. Matsushima, *J. Chem. Phys.* **83**, 1959 (1985).
- ⁵¹P. B. Merrill and R. J. Madix, *Surf. Sci.* **347**, 249 (1996).
- ⁵²G. Blyholder, J. Head, and F. Ruette, *Surf. Sci.* **131**, 403 (1983).
- ⁵³M. J. S. Spencer, A. Hung, I. K. Snook, and I. Yarovsky, *Surf. Sci.* **513**, 389 (2002).
- ⁵⁴R. A. Oriani, *Acta Metall.* **18**, 147 (1970).
- ⁵⁵A. McNabb and P. K. Foster, *Trans. Metall. Soc. AIME* **227**, 618 (1963).
- ⁵⁶J. P. Hirth and J. Lothe, *Theory of Dislocations*, 2nd ed. (Krieger, Malabar, Florida, 1992).
- ⁵⁷S. J. Plimpton, *J. Comput. Phys.* **117**, 1 (1995).